European Journal of Mechanics / A Solids 93 (2022) 104495

Contents lists available at ScienceDirect

European Journal of Mechanics / A Solids

journal homepage: www.elsevier.com/locate/ejmsol

Thermal stresses in rectangular concrete beams, resulting from constraints at microstructure, cross-section, and supports

Hui Wang [a], Yong Yuan [b], Herbert A. Mang [c,b], Qing Ai [a], Xingchun Huang [a], Bernhard L.A. Pichler [c,*]

[a] School of Naval Architecture, Ocean and Civil Engineering, Shanghai Jiao Tong University, Shanghai 200240, China
[b] College of Civil Engineering, Tongji University, Shanghai 200092, China
[c] Institute for Mechanics of Materials and Structures, TU Wien, Karlsplatz 13/202, 1040 Vienna, Austria

ARTICLE INFO

Keywords:
Thermal stresses
Multiscale analysis
Concrete beams
Constraints
Eigenstrains

ABSTRACT

Concrete beams carrying flat roofs are subjected to daily temperature cycles. Thermal eigenstrains at different scales of observation may be constrained or even prevented. This may apply to the entire beam and its support conditions, to the cross-sections of the beam, the microstructure of concrete, consisting of coarse aggregates embedded in a mortar matrix, and to the microstructure of mortar, consisting of fine aggregates embedded in a cement paste matrix. Scale transitions from the entire beam to the cross-sectional scale and further down to the microstructural scales of concrete and mortar are based on standard equations of the linear theory of slender beams and on the concentration-influence relations between the macroscopic and the microscopic strains, taken from continuum micromechanics. This multiscale approach is used for computing thermal stresses of concrete and of its constituents. Sensitivity analyses are carried out w.r.t. the support conditions, the type of coarse aggregates, the internal relative humidity, the speed of the temperature change, and the height of the cross-section. It is demonstrated that even if thermal stresses appear to be reasonably small at the scale of concrete, there may be significant microstructural stress fluctuations. They are the larger, the greater the difference between the thermo-elastic properties of the individual microstructural constituents. It is concluded that the thermal insulation of flat roofs, as promoted by the United Nations environment program to reduce energy consumption in buildings, is also important to obtain smaller daily cycles of stresses of beams carrying flat roofs.

1. Introduction

Concrete structures are frequently exposed to the ambient weather and, thus, to recurrent cycles of temperature and humidity (Jeong and Zollinger, 2005). It is well known that the corresponding stresses may lead to cracking of concrete (Grasley, 2003; Belshe et al., 2010; Wang et al., 2018a, 2019a), entailing the decrease of the durability of such structures (ACI, 2016; Zhao et al., 2020). Experimental studies have provided interesting insight into this topic. E.g., the effect of environmental thermal fatigue on the modulus of elasticity and the compressive strength was studied by Huang et al. (2019). Damage of the material, resulting in the decrease of the elastic stiffness of concrete under periodic temperature–humidity action, was investigated by Chen et al. (2020). These studies have underlined that damage of concrete originates from the microstructure. This provides the motivation for the present study, which is devoted to multiscale stress analysis of concrete beams subjected to thermal loading.

Changes of temperature result in eigenstrains. They are also referred to as "stress-free strains", because thermal stresses will not be activated if eigenstrains are free to develop. However, if they are constrained or prevented, thermal stresses will be activated. It is a central aim of the present paper to emphasize that thermal eigenstrains are constrained or prevented at three different scales of observation of concrete beams, namely, at the microstructural scale of concrete, the cross-sectional scale of a beam, and at its macrostructural scale:

1. Constraints at the microstructural scale of concrete result from the mismatch of the thermal expansion coefficients of the cement paste, the fine aggregates ("sand"), and the coarse aggregates (Fu et al., 2004; Wang et al., 2019b).
2. Constraints at the cross-sectional scale of a beam are the consequence of the fact that cross-sections remain virtually plane even if the beam is subjected to thermal loading.

* Corresponding author.
E-mail address: Bernhard.Pichler@tuwien.ac.at (B.L.A. Pichler).

https://doi.org/10.1016/j.euromechsol.2021.104495
Received 14 July 2021; Received in revised form 10 December 2021; Accepted 20 December 2021
Available online 10 January 2022

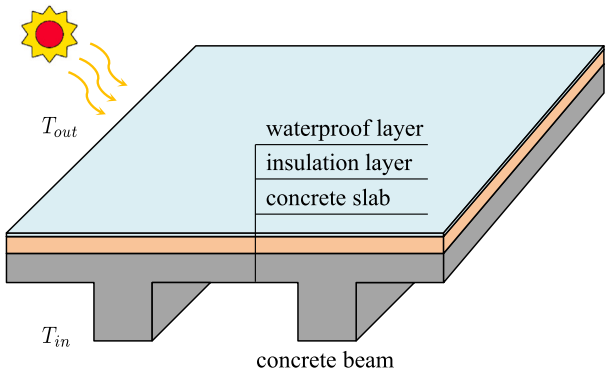

Fig. 1. Inspiration for the present multiscale analysis: flat roof, carried by rectangular concrete beams, subjected to solar heating.

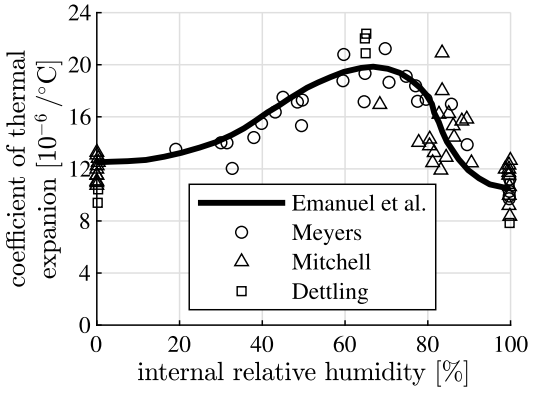

Fig. 2. Coefficient of thermal expansion of the hardened cement paste as a function of the internal relative humidity, see (Emanuel and Hulsey, 1977) and (Wang et al., 2018b).

3. Constraints at the macrostructural scale of a beam follow from the support conditions, provided that the beam is supported in a statically indeterminate fashion.

Steel reinforcements of concrete beams have almost no influence on the thermal stresses because the thermal expansion coefficient of concrete is very similar to that of steel, see e.g. (Wang et al., 2018a). Therefore, steel reinforcements are not explicitly considered in the present paper.

The multiscale nature of the described problem is addressed by means of the following methods for scale transitions:

1. As for the scale transition from the cement paste, the fine aggregates, and the coarse aggregates to the material scale of concrete, methods from continuum micromechanics are used. Phase strain concentration tensors and phase-pair eigenstrain influence tensors are estimated according to the transformation field analysis (Dvorak, 1992), using a generalized Mori–Tanaka–Benveniste scheme (Pichler and Hellmich, 2010). Corresponding analytical formulae for these estimates are taken from (Wang et al., 2019b).
2. As for the transition from the material scale of concrete to the cross-sectional scale of a beam, the kinematics of the Bernoulli beam theory is combined with Hooke's law and the stress resultants "normal force" and "bending moment". This results in analytical formulae, suggesting that the thermal eigenstrains should be split up into eigenstretches and eigencurvatures of the axis of the beam and into eigendistortions of the cross-sections, for the purpose of accounting for constraints at different scales of observation.

Combining the described methods allows for quantifying fluctuations of microstructural stresses at the scale of the cement paste, the fine aggregates, and the coarse aggregates.

In the present paper, the described mode of multiscale analysis is applied to a rectangular concrete beam, heated at its top surface, inspired by flat roofs of buildings, see Fig. 1. One aim of this analysis is to demonstrate that adequate insulation of flat roofs, as promoted by the United Nations environment program to reduce energy consumption in buildings (Berardi, 2017), is also beneficial to the reduction of the amplitude of daily stress cycles, resulting from diurnal changes of the external temperature. In this context, four types of sensitivity analyses are performed. They refer to different speeds of temperature changes to which a concrete beam is subjected, to three types of coarse aggregates with different thermoelastic properties (limestone, granite, and quartzite), to different states of internal relative humidity, resulting in different thermal expansion coefficients of the cement paste (Wang et al., 2018b), see also Fig. 2, and to different heights of the cross-section of the concrete beam. Constraints resulting from the monolithic connection between the beams and the slabs are important for calculation of stresses resulting from dead load and service loads. The thermoelastic analysis of the present study, focused on vertical heat transfer from the top of the slab in the direction to the bottom of the beam, however, is not influenced by these constraints.

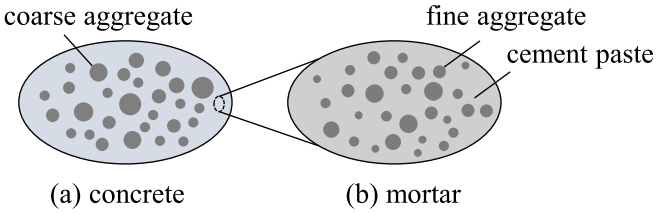

Fig. 3. Material organogram of concrete: (a) concrete consisting of coarse aggregates, embedded in a mortar matrix, and (b) mortar consisting of fine aggregates, embedded in a cement paste matrix; two-dimensional sketches of three-dimensional representative volume elements; see (Wang et al., 2019b).

The paper is structured as follows. In Section 2, analytical formulae for scale transitions from the microstructural scale of concrete to the cross-sectional scale of a beam are presented. Section 3 contains the macrostructural part of the analysis. It includes the solution of the heat transfer problem and leads to the thermal stresses at the cross-sectional level. Section 4 refers to the microstructural part of the analysis, leading to the thermal stresses experienced by the constituents of concrete. Section 5 is devoted to sensitivity analyses. Section 6 contains a discussion and the conclusions drawn from the analysis results.

2. Scale transitions regarding the thermoelastic behavior of concrete beams

2.1. Transition from the microstructural scale to the material scale of concrete

Concrete is a hierarchically organized heterogeneous material consisting of cement paste, fine aggregates, and coarse aggregates. Modeling is focused on key features of the microstructure. Concrete is modeled as spherical coarse aggregates embedded in a mortar matrix, see Fig. 3(a). Mortar is modeled as spherical fine aggregates embedded in a cement paste matrix, see Fig. 3(b). Representative volume elements of mortar and concrete, V_{RVE}, are conceptually subdivided into the matrix (index m) and the inclusions (index i), occupying the volumes V_m

and V_i, respectively. Both material phases, $p \in [\,m\,,\,i\,]$, exhibit specific properties in terms of the elastic stiffness $\mathbb{C}_p$, the eigenstrain $\boldsymbol{\varepsilon}_p^e$, and the volume fraction f_p:

$$\forall \underline{x} \in V_p \;:\; \begin{cases} \mathbb{C}(\underline{x}) = \mathbb{C}_p \\ \boldsymbol{\varepsilon}^e(\underline{x}) = \boldsymbol{\varepsilon}_p^e \end{cases}, \quad f_p = \frac{V_p}{V_{RVE}}, \quad p \in [\,m\,,\,i\,]\,. \tag{1}$$

All constituents are isotropic. Their elastic stiffness tensors $\mathbb{C}_p$ depend on their bulk moduli k_p and shear moduli μ_p:

$$\mathbb{C}_p = 3\,k_p\,\mathbb{I}_{vol} + 2\,\mu_p\,\mathbb{I}_{dev}\,, \quad p \in [\,m\,,\,i\,]\,, \tag{2}$$

where $\mathbb{I}_{vol}$ and $\mathbb{I}_{dev}$ stand for the volumetric and deviatoric part, respectively, of the symmetric fourth-order identity tensor $\mathbb{I}$. In the context of thermoelasticity, the eigenstrains $\boldsymbol{\varepsilon}_p^e$ are proportional to the product of their thermal expansion coefficient α_p and the temperature change ΔT, i.e.

$$\boldsymbol{\varepsilon}_p^e = \alpha_p\,\Delta T\,\mathbf{1}\,, \quad p \in [\,m\,,\,i\,]\,, \tag{3}$$

where $\mathbf{1}$ denotes the second-order identity tensor.

Scale transitions are based on the transformation field analysis of continuum micromechanics (Dvorak, 1992), using a generalized Mori–Tanaka–Benveniste scheme (Pichler and Hellmich, 2010). Bottom-up scale transition yields estimates of the homogenized bulk modulus, k_{hom}, the homogenized shear modulus, μ_{hom}, and the homogenized coefficient of thermal expansion, α_{hom}, as (Wang et al., 2019b)

$$k_{\text{hom}} = \frac{f_i\,k_i\left[1+\frac{3(k_i-k_m)}{3\,k_m+4\,\mu_m}\right]^{-1} + f_m\,k_m}{f_i\left[1+\frac{3(k_i-k_m)}{3\,k_m+4\,\mu_m}\right]^{-1} + f_m}\,, \tag{4}$$

$$\mu_{\text{hom}} = \frac{f_i\,\mu_i\left[1+\frac{6\,(k_m+2\,\mu_m)\,(\mu_i-\mu_m)}{5\,\mu_m(3\,k_m+4\,\mu_m)}\right]^{-1} + f_m\,\mu_m}{f_i\left[1+\frac{6\,(k_m+2\,\mu_m)\,(\mu_i-\mu_m)}{5\,\mu_m(3\,k_m+4\,\mu_m)}\right]^{-1} + f_m}\,, \tag{5}$$

$$\alpha_{\text{hom}} = \frac{3\,k_i\,k_m\,(\alpha_m\,f_m + \alpha_i\,f_i) + 4\,\mu_m\,(\alpha_m\,f_m\,k_m + \alpha_i\,f_i\,k_i)}{3\,k_i\,k_m + 4\,\mu_m\,(f_m\,k_m + f_i\,k_i)}\,. \tag{6}$$

Top-down scale transition provides access to volume-averaged strains of the matrix and the inclusions, $\boldsymbol{\varepsilon}_m$ and $\boldsymbol{\varepsilon}_i$, respectively, based on the concentration-influence relations (Dvorak, 1992; Pichler and Hellmich, 2010)

$$\boldsymbol{\varepsilon}_p = \mathbb{A}_p : \mathbf{E}_{\text{hom}} + \sum_{q=m,i} \mathbb{D}_{pq} : \boldsymbol{\varepsilon}_q^e\,, \quad p \in [\,m\,;\,i\,]\,, \tag{7}$$

where $\mathbb{A}_p$ denotes the strain concentration tensor of material phase p and $\mathbb{D}_{pq}$ stands for the influence tensor, allowing for quantification of the influence of the eigenstrain in the material phase q on the total strain of phase p, see the Appendix for details. $\mathbf{E}_{\text{hom}}$ denotes the macrostrain of the composite, which is a function of the macrostress $\boldsymbol{\Sigma}_{\text{hom}}$ and the temperature change ΔT:

$$\mathbf{E}_{\text{hom}} = \mathbb{C}_{\text{hom}}^{-1} \;:\; \boldsymbol{\Sigma}_{\text{hom}} + \alpha_{\text{hom}}\,\Delta T\,\mathbf{1}\,, \tag{8}$$

where $\mathbb{C}_{\text{hom}}^{-1}$ is the inverse of the homogenized stiffness tensor of the composite, with $\mathbb{C}_{\text{hom}}$ following from Eq. (2) specialized for p = hom, see also Eqs. (4) and (5). The volume-averaged stresses of the matrix and the inclusions, $\boldsymbol{\sigma}_m$ and $\boldsymbol{\sigma}_i$, follow from the generalized Hooke's law as

$$\boldsymbol{\sigma}_p = \mathbb{C}_p : (\boldsymbol{\varepsilon}_p - \boldsymbol{\varepsilon}_p^e)\,, \quad p \in [\,m\,,\,i\,]\,. \tag{9}$$

Notably, the average stresses of the matrix and of the inclusions satisfy the stress average rule:

$$\boldsymbol{\Sigma}_{\text{hom}} = f_m\,\boldsymbol{\sigma}_m + f_i\,\boldsymbol{\sigma}_i\,. \tag{10}$$

2.2. Transition from the material scale of concrete to the cross-sectional scale of a beam

If a concrete beam is subjected to transient heat conduction, changes of temperature relative to a constant reference temperature will be nonlinearly distributed across the cross-section. Related eigenstrains are equal to the product of the thermal expansion coefficient, α_{con}, and the temperature change ΔT

$$\varepsilon_{xx}^e = \varepsilon_{yy}^e = \varepsilon_{zz}^e = \alpha_{con}\,\Delta T\,. \tag{11}$$

Herein, the focus rests on heat conduction in the thickness direction, characterized by the z-coordinate.

At the cross-sectional scale, the eigenstrains (11) are subdivided into three parts: the eigenstretch and the eigencurvature of the axis of the beam, and the eigendistortion of its cross-section. In this section, it will be shown that rules for this decomposition follow from the Euler–Bernoulli hypothesis, stating that cross-sections remain plane in the deformed configuration:

$$u = u_0 - \frac{\mathrm{d}w_0}{\mathrm{d}x}\,z\,, \tag{12}$$

where u stands for the axial displacement field of the cross-section, u_0 denotes the axial displacement of the center of gravity of the cross-section, and w_0 stands for its deflection, see Fig. 4 for the coordinate system used. The axial normal stress reads as $\sigma_{xx} = E\,(\varepsilon_{xx} - \varepsilon_{xx}^e)$, where E stands for the modulus of elasticity, and ε_{xx} denotes the axial normal strain. Expressing the latter as the partial derivative of u according to Eq. (12) with respect to x, yields

$$\sigma_{xx} = E\,(\varepsilon_0 + \kappa_0\,z - \varepsilon_{xx}^e)\,, \tag{13}$$

with $\varepsilon_0 = \mathrm{d}u_0/\mathrm{d}x$ and $\kappa_0 = -\mathrm{d}^2w_0/\mathrm{d}x^2$. Insertion of Eq. (13) into the expression for the normal force, $N = \int_A \sigma_{xx}\,\mathrm{d}A$, yields both the constitutive law,

$$N = E\,A\,(\varepsilon_0 - \varepsilon_0^e)\,, \tag{14}$$

and the expression for the eigenstretch of the axis of the beam,

$$\varepsilon_0^e := \frac{1}{A}\int_A \varepsilon_{xx}^e\,\mathrm{d}A\,, \tag{15}$$

with A denoting the cross-sectional area. Similarly, insertion of Eq. (13) into the expression for the bending moment, $M = \int_A \sigma_{xx}\,z\,\mathrm{d}A$, yields both the constitutive law,

$$M = E\,I\,(\kappa_0 - \kappa_0^e)\,, \tag{16}$$

and the expression for the eigencurvature of the axis of the beam,

$$\kappa_0^e := \frac{1}{I}\int_A \varepsilon_{xx}^e\,z\,\mathrm{d}A\,, \tag{17}$$

with I denoting the cross-sectional moment of inertia. Solving Eq. (14) for ε_0 and Eq. (16) for κ_0 and inserting the resulting expressions into Eq. (13), yields the following expression for the stresses:

$$\sigma_{xx} = \frac{N}{A} + \frac{M}{I}\,z - E\,(\varepsilon_{xx}^e - \varepsilon_0^e - \kappa_0^e\,z)\,. \tag{18}$$

Eqs. (15), (17), and (18) allow for the following interpretations. The eigenstretch of the beam is equal to the cross-sectional mean value of the eigenstrain distribution, see Eq. (15). The eigencurvature of the beam is equal to the cross-sectional first moment of the eigenstrain distribution, see Eq. (17). Subtracting the constant eigenstretch part, ε_0^e, and the linear eigencurvature part, $\kappa_0^e\,z$, from the total eigenstrains, ε_{xx}^e, yields the spatially nonlinear cross-sectional eigendistortion part, see the term in the parentheses in Eq. (18). It is prevented insofar as cross-sections remain virtually plane, see Eq. (12). Thus, eigendistortions are nullified by stress-related strains of identical size and opposite sign, see the minus sign in front of the third term on the right-hand-side of Eq. (18). Multiplying the stress-related strains with the modulus of elasticity yields eigenstresses resulting from prevented cross-sectional eigendistortions. They neither contribute to the normal force nor to the bending moment, because both their mean values and first moments vanish.

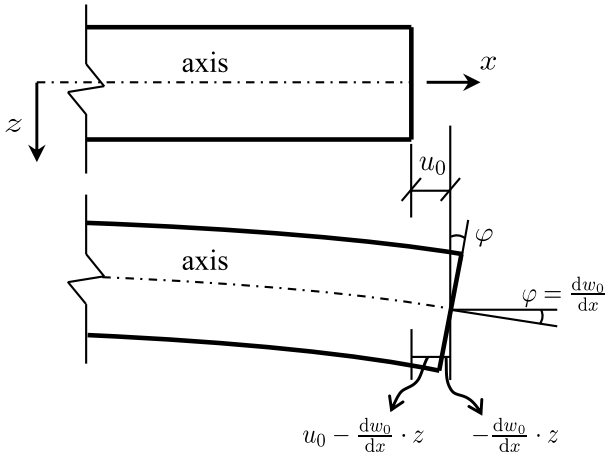

Fig. 4. Coordinate system for rectangular concrete beams; Euler–Bernoulli hypothesis.

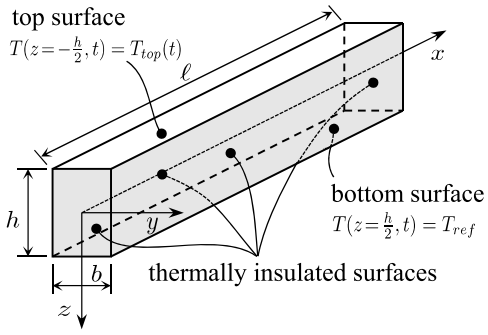

Fig. 5. Rectangular concrete beam subjected to one-dimensional heat conduction in the thickness direction.

3. Macroscopic analysis of thermal stresses in rectangular concrete beams

The described mode of multiscale analysis is applied to rectangular concrete beams (Fig. 5), subjected to heating at their top surfaces. The height, h, of the cross-section is equal to 30 cm. A sensitivity analysis, addressing larger values of h, is the topic of Section 5.4. Notably, the width of the cross-section does not affect the quantification of the thermal eigenstresses.

The analyzed beams consist of mature concrete with an initial water-to-cement mass ratio of 0.40, coarse aggregates made of granite, fine aggregates made of sandstone, and an internal relative humidity of 100%. The material properties of the constituents of concrete include volume fractions, elastic stiffness properties, and coefficients of thermal expansion, see Table 1. They are taken from (Wang et al., 2019b) for the purpose of analyzing a concrete equivalent to the one considered in (Naik et al., 2011). Upscaling based on Eqs. (4)–(6) yields homogenized thermoelastic properties of the concrete considered, see Table 1. The coefficient of thermal expansion, α_{con}, amounts to 9.27×10^{-6}/°C, and the modulus of elasticity, E_{con}, to 31.07 GPa. The latter was obtained from the homogenized bulk and shear moduli listed in Table 1, using the following standard relation for isotropic materials:

$$E_{con} = \frac{9\, k_{con}\, \mu_{con}}{3\, k_{con} + \mu_{con}}\,. \tag{19}$$

The value of the thermal diffusivity, a, of the concrete is equal to 0.85×10^{-6} m^2/s, see Bažant and Kaplan (1996).

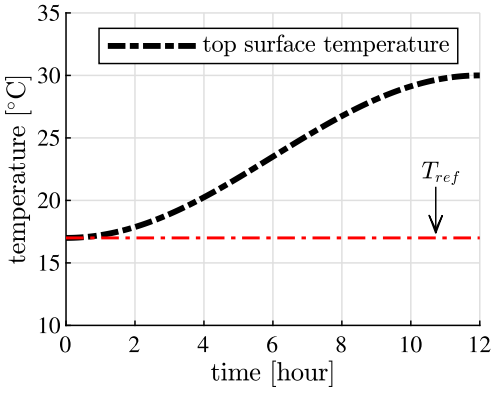

Fig. 6. Prescribed temperature evolution at the top surface of the beam.

The remainder of this section is structured as follows. After solution of the heat conduction problem, the thermal eigenstrains are computed. The related thermal stresses are determined at the scale of the cross-sections, accounting for constraints at this scale and of the entire beam structure.

3.1. Temperature fields and thermal eigenstrains

The initial conditions and the boundary conditions of the investigated problem of heat conduction read as follows. The initial configuration is isothermal at 17 °C. At the bottom of the beam, the temperature stays constant. For the sake of simplicity, it is assumed that there is no heat flux across the lateral surfaces of the beam. The temperature at the top surface is increased, during 12 h, by 13 °C, i.e. up to 30 °C, in the form of an S-shaped function of time t:

$$T_{top}(t) = 17\ ^\circ\mathrm{C} + 13\ ^\circ\mathrm{C} \cdot \frac{1}{2}\left[1 - \cos\left(\frac{t\,\pi}{12\ \mathrm{h}}\right)\right], \tag{20}$$

see also Fig. 6.

The boundary conditions result in one-dimensional heat conduction along the height of the beam. This direction is characterized by the z-coordinate, see Fig. 5. Thus, the heat equation takes the form

$$\frac{\partial T}{\partial t} - a\,\frac{\partial^2 T}{\partial z^2} = 0\,, \tag{21}$$

where $T = T(z,t)$ denotes the history of the temperature field. As for the solution of Eq. (21), the prescribed temperature history, see Eq. (20), is approximated in a step-wise fashion, with one temperature step per minute: $t_i = i \times 1$ min, with $i = 1, 2, \ldots, 720$. The corresponding temperature changes are obtained as

$$\Delta T_{top}(t_i) = T_{top}(t_i) - T_{top}(t_{i-1})\,, \qquad i = 1, 2, \ldots, 720\,, \tag{22}$$

where $T_{top}(t_i)$ and $T_{top}(t_{i-1})$ follow from Eq. (20). The solution of the heat conduction problem reads as (Wang et al., 2019a)

$$T(z,t) = 17\ ^\circ\mathrm{C} + \sum_{i=1}^{720} \Delta T_{top}(t_i) \left\{ \left(\frac{1}{2} - \frac{z}{h}\right) - \sum_{n=1}^{\infty} \frac{(-1)^n}{n\,\pi} \sin\left(2\,n\,\pi\,\frac{z}{h}\right) \exp\left[-(2\,n\,\pi)^2 \frac{a\,\langle t - t_i\rangle}{h^2}\right] + \sum_{n=1}^{\infty} \frac{2\,(-1)^n}{(2\,n-1)\,\pi} \cos\left[(2\,n-1)\,\pi\,\frac{z}{h}\right] \exp\left[-(2\,n-1)^2\,\pi^2\,\frac{a\,\langle t - t_i\rangle}{h^2}\right] \right\}, \tag{23}$$

where h denotes the height of the beam, and $\langle\cdot\rangle$ denotes the Macaulay operator. $\langle t - t_i\rangle$ is defined as $(t - t_i + |t - t_i|)/2$. The infinite sums in

Table 1
Upscaling of thermoelastic properties of mortar and concrete; computed by means to Eqs. (4)–(6); input values are printed in bold face.

Material	Volume fraction [–]	Bulk modulus [GPa]	Shear modulus[GPa]	Thermal expansion coefficient [10^{-6}/°C]
Cement paste ($w/c = 0.40$)	**0.545**	**13.11**	**9.83**	**10.50**
Fine aggregate (sandstone)	**0.455**	**23.33**	**14.00**	**11.25**
Homogenized mortar	–	16.94	11.53	10.89
Material	Volume fraction [–]	Bulk modulus [GPa]	Shear modulus [GPa]	Thermal expansion coefficient [10^{-6}/°C]
Mortar (homogenized)	**0.55**	**16.94**	**11.53**	**10.89**
Coarse aggregate (granite)	**0.45**	**21.61**	**14.23**	**7.50**
Homogenized concrete	–	18.89	12.67	9.27

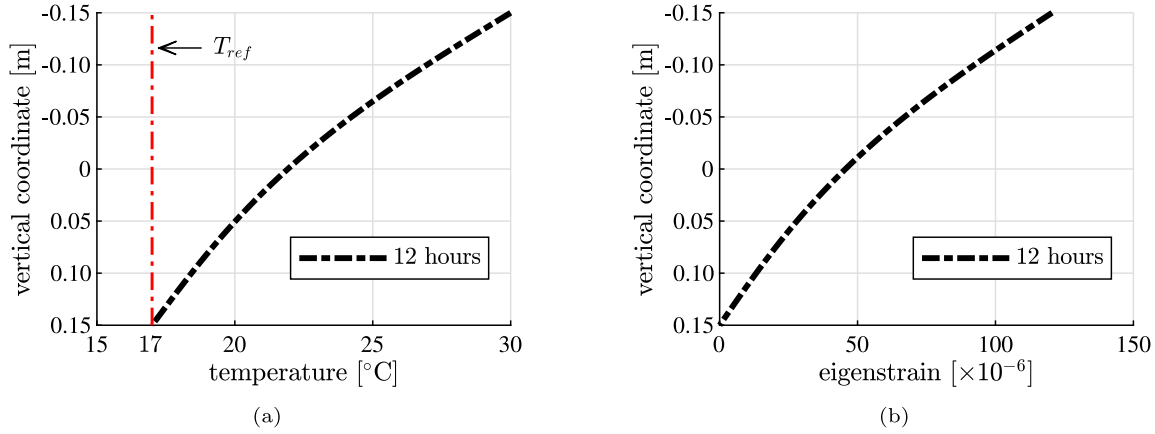

Fig. 7. Distribution of (a) the temperature and (b) the thermal eigenstrain across the height of the beam, at the end of heating of the top surface.

Eq. (23) are truncated after the first 1000 summands. This provides a well-converged solution.

A spatially nonlinear temperature distribution is obtained at the end of the heating process of 12 h, see Fig. 7 (a). Thermal eigenstrains are obtained by multiplying the temperature change, $\Delta T = T(z,t) - 17$ °C, by the thermal expansion coefficient of concrete, listed in Table 1, see Fig. 7 (b).

3.2. Decomposition of the thermal eigenstrains

The thermal eigenstrain in Fig. 7 (b) is decomposed into contributions related to an eigenstretch and an eigencurvature of the axis of the beam, and into an eigendistortion of its cross-sections. The eigenstretch and the eigencurvature follow from Eqs. (15) and (17) as (Wang et al., 2019a)

$$\varepsilon_0^e = +\sum_{i=1}^{720} \alpha_{con}\,\Delta T_{top}(t_i) \left\{ \frac{1}{2} - \sum_{n=1}^{\infty} \frac{4}{(2n-1)^2\,\pi^2} \times \exp\left[-\frac{(2n-1)^2\,\pi^2\,a\,\langle t - t_i \rangle}{h^2} \right] \right\}, \tag{24}$$

$$\kappa_0^e = -\sum_{i=1}^{720} \frac{\alpha_{con}\,\Delta T_{top}(t_i)}{h} \left\{ 1 - \sum_{n=1}^{\infty} \frac{6}{n^2\,\pi^2} \times \exp\left[-\frac{(2n\pi)^2\,a\,\langle t - t_i \rangle}{h^2} \right] \right\}. \tag{25}$$

The infinite sums in Eqs. (24) and (25) are truncated after the first 1000 summands. This provides well-converged solutions. As for the time instant at the end of heating ($t = 12$ h), the numerical values of the eigenstretch and the eigencurvature are obtained as $\varepsilon_0^e = 5.09 \times 10^{-5}$ and $\kappa_0^e = -3.97 \times 10^{-4}$ m^{-1}, respectively. Subtracting the constant eigenstretch part, ε_0^e, and the linear eigencurvature part, $\kappa_0^e\,z$, from the total eigenstrain, ε_{xx}^e, leads to the spatially nonlinear eigendistortions of the cross-sections: $\varepsilon_{xx}^e - \varepsilon_0^e - \kappa_0^e\,z$, see Fig. 8 (a).

3.3. Thermal stresses at the cross-sectional level

Eigendistortions are prevented at the scale of the cross-sections because, according to the Euler–Bernoulli hypothesis, they remain virtually plane even under transient thermal loading. The corresponding stresses are obtained from the last term in Eq. (18), see Fig. 8 (b).

Whether eigenstretches and eigendistortions are free to develop, constrained, or prevented depends on the support conditions of the beam. They are free to develop in statically determinate beams, constrained in statically indeterminate beams, and prevented in beams clamped at both ends. Thus, there are lower and upper bounds of the absolute values of the normal force N and the bending moment M. The lower bounds (index "lb"), referring to statically determinate beams, are equal to zero: $N_{lb} = 0$ and $M_{lb} = 0$. The upper bounds (index "ub"), referring to double-clamped beams, follow from Eqs. (14) and (16) by setting ε_0 and κ_0 equal to zero:

$$N_{ub} = -E\,A\,\varepsilon_0^e, \quad M_{ub} = -E\,I\,\kappa_0^e. \tag{26}$$

Corresponding cross-sectional normal stresses follow from Eq. (18). They are shown in Fig. 9.

4. Multiscale analysis: microscopic thermal stresses

When concrete is subjected to *temperature changes*, microscopic thermal stresses are activated because the coarse aggregates, the fine aggregates, and the cement paste have different coefficients of thermal expansion. Also, when concrete is subjected to *stresses*, microscopic stress fluctuations are activated, because the three microstructural constituents have different elastic stiffness properties. This provides the

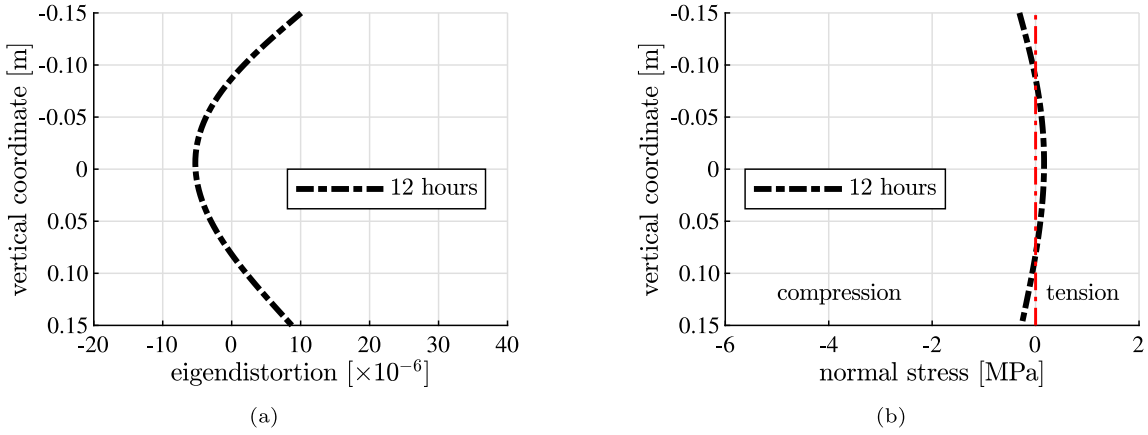

Fig. 8. Distribution of (a) the eigendistortions of the cross-sections and (b) the corresponding thermal stresses of concrete across the height of the beam, at the end of heating of the top surface.

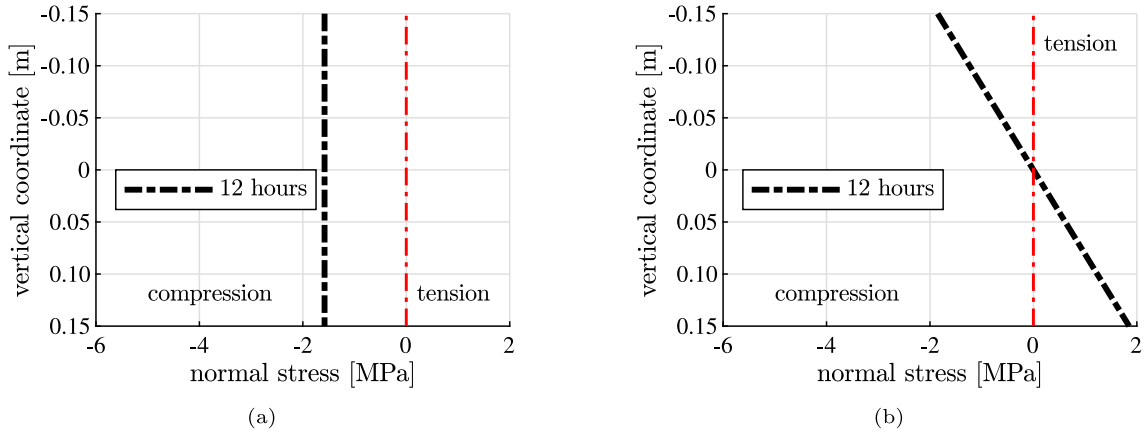

Fig. 9. Distribution of thermal stresses resulting from prevented (a) eigenstretches and (b) eigencurvatures in double-clamped beams across the height of the beam, at the end of heating of the top surface.

motivation to compute, in a step-by-step fashion, the microstresses resulting from the temperature change, the prevented eigendistortions of the cross-sections, and the prevented eigenstretch and eigencurvature of the beam.

4.1. Flow of the calculation procedure

The procedure of the calculation of the thermal stresses is summarized as follows:

1. Quantification of the elastic stiffness and the thermal expansion coefficient of concrete based on thermoelastic properties and volume fractions of the microstructural constituents, see Eqs. (4)–(6) and (19).
2. Determination of the evolution of the temperature field according to Eq. (23).
3. Computation of the thermal eigenstrains ε^e_{xx} according to Eq. (11).
4. Decomposition of the thermal eigenstrains: Calculation of
   - the eigenstretch ε^e_0 according to Eq. (24),
   - the eigencurvature κ^e_0 according to Eq. (25), and
   - the eigendistortions as $\varepsilon^e_{xx} - \varepsilon^e_0 - \kappa^e_0\, z$.
5. Quantification of the thermal eigenstresses at the cross-sectional level as: $-E\,(\varepsilon^e_{xx} - \varepsilon^e_0 - \kappa^e_0\, z)$.
6. Computation of the microscopic thermal stresses by means of top-down scale transition, see Eqs. (7)–(9) and the Appendix.

The mentioned formulae can be evaluated simply, using software for numerical calculus. In the present study, MATLAB (The Mathworks, Inc., 2020) is used.

4.2. Microscopic stresses resulting from the temperature change

The first downscaling step leads from "macroscopic" or "homogenized" concrete to the mortar matrix and the coarse aggregate inclusions. Because of the focus on the influence of the temperature change, the macrostresses of concrete are set equal to zero: $\boldsymbol{\Sigma}_{\text{hom}}(=\boldsymbol{\Sigma}_{con}) = 0$. The homogenized thermal expansion coefficient is the one of concrete: $\alpha_{\text{hom}} = \alpha_{con}$, see Table 1, and the temperature change of concrete is computed as $\Delta T = T(z,t) - 17$ °C, with $T(z,t)$ taken from Fig. 7 (a). The macrostrains $\boldsymbol{E}_{\text{hom}}(=\boldsymbol{E}_{con})$ are obtained from Eq. (8), and the eigenstrains $\boldsymbol{\varepsilon}^e_m(=\boldsymbol{\varepsilon}^e_{mor})$ and $\boldsymbol{\varepsilon}^e_i(=\boldsymbol{\varepsilon}^e_{cagg})$ are obtained from Eq. (3). Inserting them into Eq. (7) yields the average strains $\boldsymbol{\varepsilon}_m(=\boldsymbol{\varepsilon}_{mor})$ and $\boldsymbol{\varepsilon}_i(=\boldsymbol{\varepsilon}_{cagg})$. Finally, the average stresses $\boldsymbol{\sigma}_m(=\boldsymbol{\sigma}_{mor})$ and $\boldsymbol{\sigma}_i(=\boldsymbol{\sigma}_{cagg})$ are obtained from inserting the computed strains into Eq. (9). This downscaling yields isotropic tensile stresses of the coarse aggregates

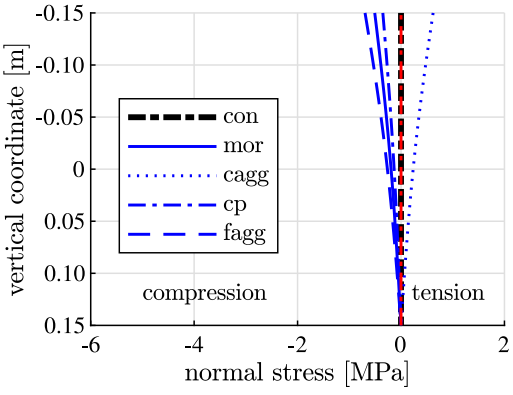

Fig. 10. Microstresses resulting from the temperature changes illustrated in Fig. 7(a) across the height of the beam, at the end of heating of the top surface: con = concrete, mor = mortar, cagg = coarse aggregates, cp = cement paste, fagg = fine aggregates.

and isotropic compressive stresses of mortar, see Fig. 10, because the larger expansion of the mortar matrix is constrained by the smaller expansion of the coarse aggregates (Table 1). No stresses are activated at the bottom of the beam, noting that the temperature remains constant there. The microscopic stresses increase from the bottom to the top of the beam, since the temperature change increases with increasing vertical distance from the bottom of the beam. Inserting the average stresses of mortar and coarse aggregates together with their volume fractions (Table 1) into the stress average rule, see Eq. (10), yields vanishing macrostresses of concrete $\boldsymbol{\Sigma}_{\text{hom}}(= \boldsymbol{\Sigma}_{con}) = 0$. This underlines that the microstresses of the mortar and the coarse aggregates "fluctuate" around the macrostresses of concrete.

The second downscaling step leads from "macroscopic" or "homogenized" mortar to the cement paste matrix and the fine aggregate inclusions. This time, the macrostress is equal to average stress of mortar obtained from the first downscaling step: $\boldsymbol{\Sigma}_{\text{hom}} = \boldsymbol{\sigma}_{mor}$. The homogenized thermal expansion coefficient is the one of mortar: $\alpha_{\text{hom}} = \alpha_{mor}$, see Table 1. The temperature changes are taken from above. $\boldsymbol{E}_{\text{hom}}$ is equal to $\boldsymbol{\varepsilon}_{mor}$ from the first downscaling step. The eigenstrains $\boldsymbol{\varepsilon}^e_m(= \boldsymbol{\varepsilon}^e_{cp})$ and $\boldsymbol{\varepsilon}^e_i(= \boldsymbol{\varepsilon}^e_{fagg})$ are computed according to Eq. (3). Inserting them into Eq. (7) yields the average strains $\boldsymbol{\varepsilon}_m(= \boldsymbol{\varepsilon}_{cp})$ and $\boldsymbol{\varepsilon}_i(= \boldsymbol{\varepsilon}_{fagg})$. Finally, the average stresses $\boldsymbol{\sigma}_m(= \boldsymbol{\sigma}_{cp})$ and $\boldsymbol{\sigma}_i(= \boldsymbol{\sigma}_{fagg})$ are obtained from inserting the computed strains into Eq. (9). This downscaling yields isotropic compressive stresses of the fine aggregates and the cement paste, which "fluctuate" around the macrostresses of mortar, see Fig. 10. The compressive stresses of the fine aggregates are larger than those of the cement paste, because their coefficients of thermal expansion are almost the same, but the bulk modulus of the fine aggregates is significantly larger than that of the cement paste. This is a consequence of the *statically indeterminate nature* of the microstructure of mortar. This expression implies that the computation of the microscopic stresses must not be restricted to the equilibrium conditions, but must also include conditions of strain compatibility. This leads to the well known effect that stiffer (micro)structural elements, i.e. fine aggregates, attract a larger share of the load than more compliant (micro)structural elements, i.e. the cement paste matrix.

4.3. Microscopic stresses resulting from prevented eigendistortions of the cross-sections of the beam

For computation of the microscopic stresses resulting from prevented eigendistortions of the cross-sections, the macrostress of concrete is needed. It is given as $\boldsymbol{\Sigma}_{\text{hom}} = -E_{con}\left(\alpha_{con}\Delta T - \varepsilon^e_0 - \kappa^e_0 z\right)(\mathbf{e}_x \otimes \mathbf{e}_x)$, with $E_{con} = 31.06$ GPa, $\varepsilon^e_0 = 5.09 \times 10^{-5}$, and $\kappa^e_0 = -3.97 \times 10^{-4}$ m^{-1}, see also Fig. 8(b). Thermal eigenstrains were already analyzed in the preceding subsection. Therefore, they are equal to zero herein: $\boldsymbol{\varepsilon}^e_{con} = \boldsymbol{\varepsilon}^e_{cagg} = \boldsymbol{\varepsilon}^e_{mor} = \boldsymbol{\varepsilon}^e_{fagg} = \boldsymbol{\varepsilon}^e_{cp} = 0$.

Both downscaling steps are governed by contrasts of stiffness. Because the coarse aggregates are stiffer than the mortar, the absolute values of the stresses of the coarse aggregates are slightly larger than those of the mortar. The stresses of the concrete are in between. Because the fine aggregates are stiffer than the cement paste, the absolute values of their stresses are slightly larger than those of the cement paste. The stresses of the mortar are in between. Notably, the stress fluctuations resulting from the prevented eigendistortions of the cross-sections are significantly smaller than those resulting from the temperature change, compare Figs. 11 and 10.

4.4. Microscopic stresses resulting from the prevented eigenstretch and eigencurvature of a double-clamped beam

For computation of the microscopic stresses resulting from the prevented eigenstretch and eigencurvature of a beam clamped at both ends, the macrostress of concrete is needed. It is given as $\boldsymbol{\Sigma}_{\text{hom}} = \left(\frac{N_{ub}}{A} + \frac{M_{ub}}{I} z\right)(\mathbf{e}_x \otimes \mathbf{e}_x)$, see Fig. 9. The thermal eigenstrains are equal to zero: $\boldsymbol{\varepsilon}^e_{con} = \boldsymbol{\varepsilon}^e_{cagg} = \boldsymbol{\varepsilon}^e_{mor} = \boldsymbol{\varepsilon}^e_{fagg} = \boldsymbol{\varepsilon}^e_{cp} = 0$. Again, both downscaling steps are governed by contrasts of stiffness. For the results, see Fig. 12.

4.5. Bounding scenarios: statically determinate beam and double-clamped beam

Microscopic stresses resulting from the temperature change (Fig. 10) and from the prevented eigendistortions of the cross-sections (Fig. 11) are inevitable. The superposition of these two contributions yields the total effective stresses in statically determinate beams, see Fig. 13(a). The effective stresses in a (statically indeterminate) double-clamped beam contain all of the three contributions, namely, the one from the temperature change (Fig. 10), the prevented eigendistortions of the cross-sections (Fig. 11), and the prevented eigenstretch and eigencurvature of the beam (Fig. 12), see Fig. 13(b).

5. Sensitivity analyses

The results from multiscale analysis presented so far refer to mature concrete with coarse aggregates made of granite and to an internal relative humidity of 100%, resulting in thermoelastic properties listed in Table 1. The duration of heating amounted to 12 h. Four types of sensitivity analyses are carried out. One of them refers to the type of the coarse aggregates. The other ones are related to the internal relative humidity, the speed of the heating process, and the height of the concrete beam. Without loss of generality, the discussion is limited to stresses in statically determinate beams.

5.1. Sensitivity analysis regarding the type of coarse aggregates

In order to study the role of the coarse aggregates, granite is replaced by limestone and quartzite, respectively, see Table 2. All other properties of the problem at hand stay the same as in Section 4. Limestone is stiffer and less expansive than granite. Quartzite is even stiffer than limestone and more expansive than granite.

Macroscopic thermal stresses of concrete, resulting from the prevented eigendistortions, given as $\boldsymbol{\Sigma}_{\text{hom}} = -E_{con}\left(\alpha_{con}\Delta T - \varepsilon^e_0 - \kappa^e_0 z\right)(\mathbf{e}_x \otimes \mathbf{e}_x)$, are proportional to the product of the thermal expansion coefficient of concrete and its modulus of elasticity, see also Eqs. (24) and (25) as well as Table 2. As for granite, limestone, and quartzite, these products amount to 288×10^{-6} GPa/°C, 268×10^{-6} GPa/°C, and 411×10^{-6} GPa/°C, respectively. This explains why granite and limestone result in virtually the same stresses at the level of concrete, while quartzite yields larger stresses, see Fig. 14(a).

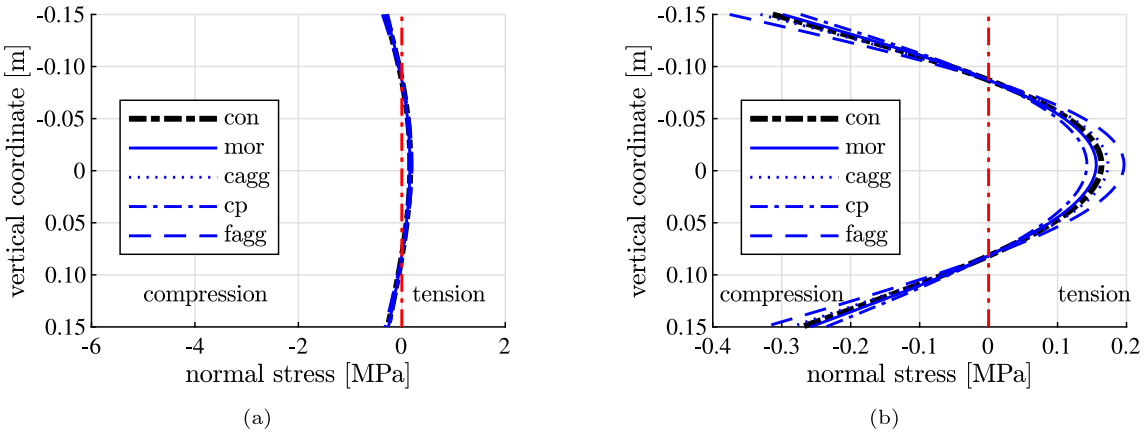

Fig. 11. Microscopic normal stress resulting from prevented eigendistortions of the cross-sections of the beam, across the height of the beam, at the end of heating of the top surface: con = concrete, mor = mortar, cagg = coarse aggregates, cp = cement paste, fagg = fine aggregates: (a) results presented in a stress interval allowing for direct comparison with Figs. 10 and 12, (b) detail of the left diagram, with a smaller stress interval.

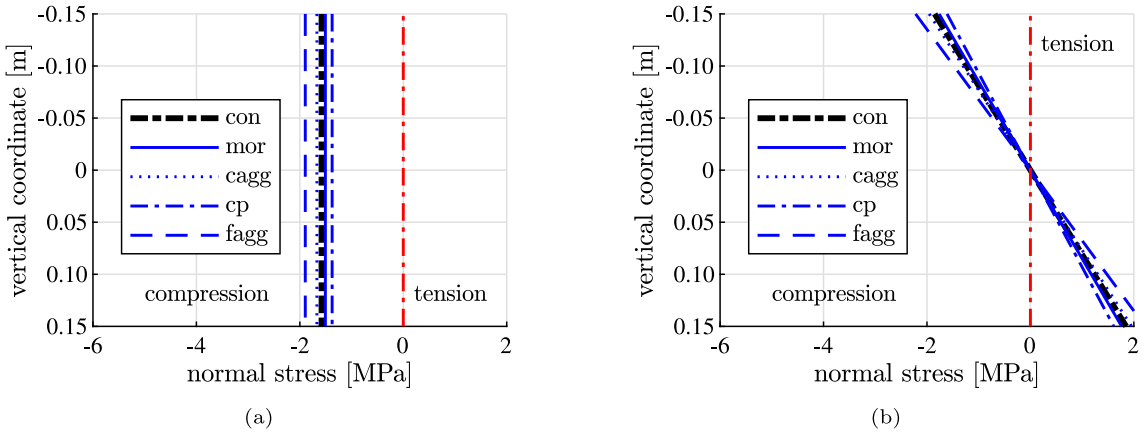

Fig. 12. Microscopic normal stress resulting from prevented (a) eigenstretches and (b) eigencurvatures in double-clamped beams across the height of the beam, at the end of heating of the top surface: con = concrete, mor = mortar, cagg = coarse aggregates, cp = cement paste, fagg = fine aggregates.

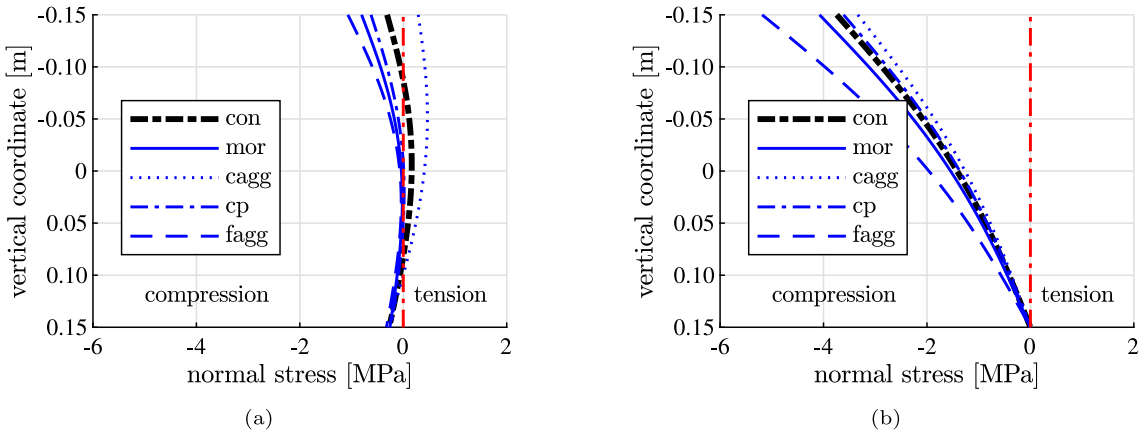

Fig. 13. Effective microscopic normal stress of (a) statically determinate beams and (b) double-clamped beams across their heights, at the end of heating of the top surface: con = concrete, mor = mortar, cagg = coarse aggregates, cp = cement paste, fagg = fine aggregates.

Table 2
Sensitivity analysis regarding the type of coarse aggregates: thermoelastic properties of the three types of coarse aggregates considered and of the corresponding concretes.

Coarse aggregate	k_{cagg} [GPa]	μ_{cagg} [GPa]	α_{cagg} [10^{-6}/°C]	E_{con} [GPa]	α_{con} [10^{-6}/°C]
Limestone	32.61	17.72	4.75	34.71	7.73
Granite	21.61	14.23	7.50	31.07	9.27
Quartzite	24.51	21.55	11.75	36.33	11.31

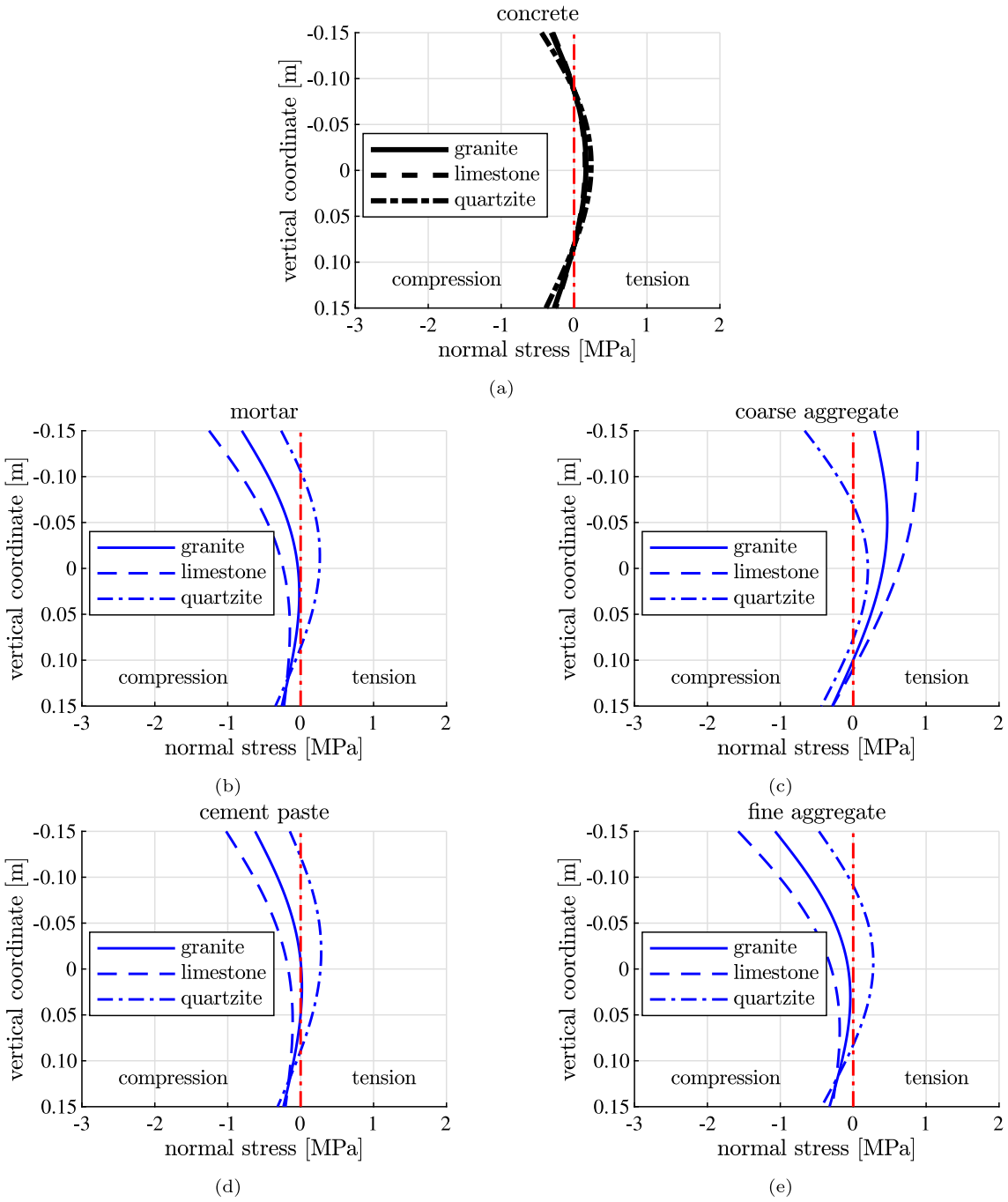

Fig. 14. Results from sensitivity analysis regarding the type of coarse aggregates: normal stresses in (a) the concrete, (b) the mortar, (c) the coarse aggregates, (d) the cement paste, and (e) the fine aggregates across the height of a statically determinate beam, at the end of twelve-hour heating of the top surface.

Stresses in the coarse aggregates and in the mortar, see Fig. 14(b) and (c), fluctuate around the stresses in the concrete. These fluctuations are governed by the difference of stiffness and, more importantly, by differences of the thermal expansion. Each one of the three types of coarse aggregates is stiffer than the mortar matrix. Limestone and granite expand significantly less than mortar, while quartzite expands only

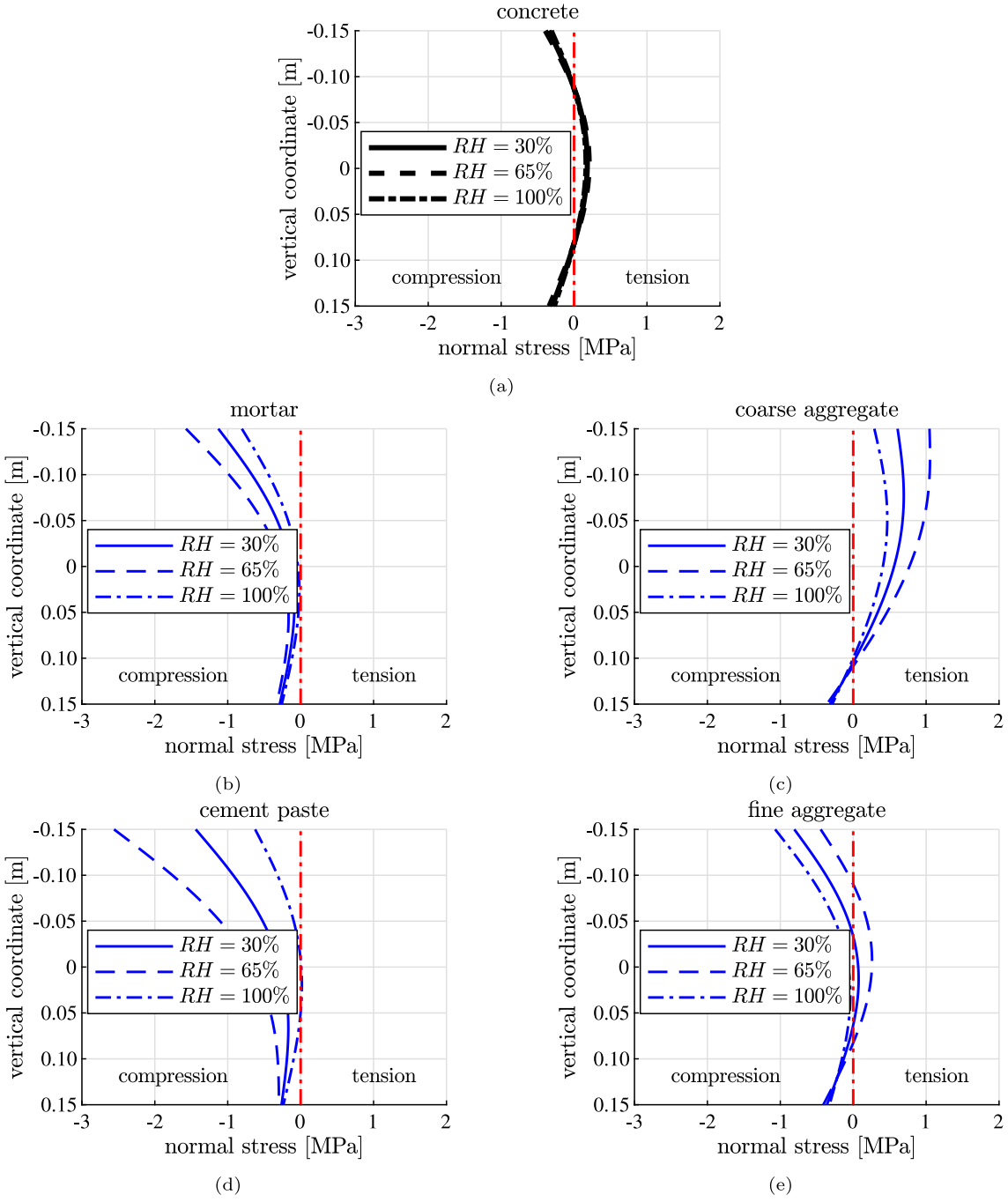

Fig. 15. Results from sensitivity analysis regarding the internal relative humidity: normal stresses in (a) the concrete, (b) the mortar, (c) the coarse aggregates, (d) the cement paste, and (e) fine aggregates across the height of a statically determinate beam, at the end of twelve-hour heating of the top surface.

slightly more than mortar, compare Tables 1 and 2. These properties result in differences between the stresses in quartzite and mortar, which are significantly smaller than the differences between the stresses in granite and mortar. The differences between the stresses in limestone and mortar are the largest, because of the particularly large difference of their coefficients of thermal expansion.

Stresses in the fine aggregates and the cement paste, see Fig. 14(d) and (e), fluctuate around the stresses in the mortar. Each one of the three concretes analyzed is made of the same types of small aggregates and cement paste. Therefore, the magnitude of the stress *fluctuations* around the stresses of the mortar is similar in the three investigated cases. Still, because the stresses of the mortar strongly depend on the type of the coarse aggregates, see Fig. 14(b), also the stresses in the fine aggregates and in the cement paste are different for different concretes.

5.2. Sensitivity analysis regarding the internal relative humidity

So far, the relative humidity was assumed to be equal to 100%. In order to study its influence on the stresses in the investigated beam, it is now set equal to 65% and to 30%, respectively, see Table 3. The other input quantities remain the same as in Section 4. The thermal expansion coefficient of the cement paste at $RH = 65\%$ is virtually twice as large as that at $RH = 100\%$ (Emanuel and Hulsey, 1977; Wang et al., 2018b).

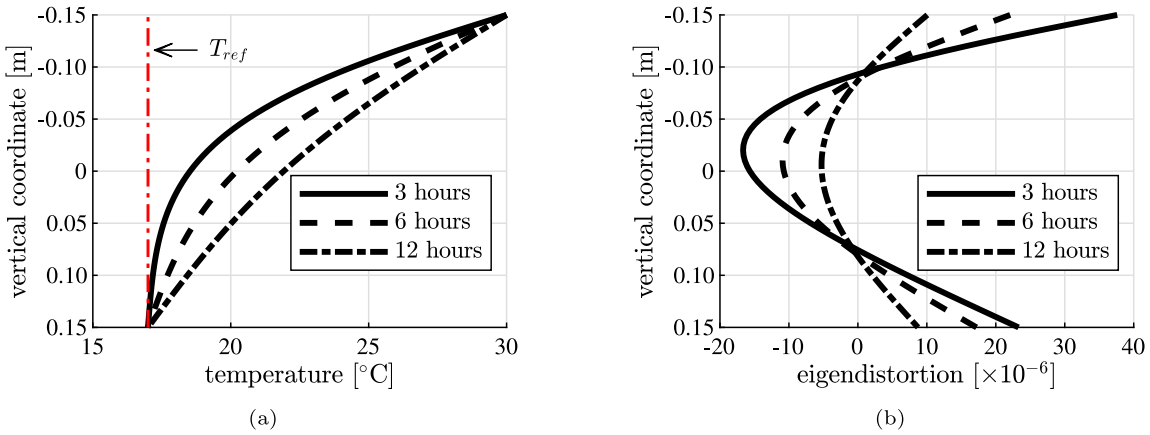

Fig. 16. Results from sensitivity analysis regarding the speed of the heating process: (a) temperature field and (b) thermal eigendistortions, across the height of the beam, at the end of three different heating processes, lasting for 12, 6, and 3 h, respectively.

Table 3
Sensitivity analysis regarding the internal relative humidity: thermal expansion coefficients of the cement paste, the mortar, and the concrete at internal relative humidities RH of 30%, 65%, and 100%, respectively.

Relative humidity	α_{cp} [10^{-6}/°C]	α_{mor} [10^{-6}/°C]	α_{con} [10^{-6}/°C]
$RH = 30\%$	14.5	12.82	10.28
$RH = 65\%$	20.0	15.48	11.68
$RH = 100\%$	10.5	10.89	9.27

Table 4
Results from sensitivity analysis regarding the speed of the heating process: eigenstretches and eigencurvatures of the axis of the beam at the end of three different heating processes, lasting for 12 h, 6 h, and 3 h, respectively.

Heating period	ϵ_0^e [–]	κ_0^e [m^{-1}]
3 h	2.98×10^{-5}	-3.54×10^{-4}
6 h	4.06×10^{-5}	-3.85×10^{-4}
12 h	5.09×10^{-5}	-3.97×10^{-4}

At $RH = 30\%$, the thermal expansion coefficient of the cement paste is approximately 1.5-times larger than that at $RH = 100\%$ (Emanuel and Hulsey, 1977; Wang et al., 2018b), see also Table 3.

A significant increase of the thermal expansion coefficient of the cement paste results in a moderate increase of the thermal expansion coefficient of mortar and in an even smaller increase of that of concrete, see Table 3. The elastic stiffness properties are independent of the RH. In other words: they are constant, see Table 1. The products of the modulus of elasticity and the thermal expansion coefficient of concrete are quite similar. Thus, the macrostresses of concrete are also quite similar for the three investigated values of the RH, see Fig. 15(a).

Stresses in the coarse aggregates and mortar, see Fig. 15(b) and (c), fluctuate around the stresses in the concrete. These fluctuations are the larger, the greater the difference between the thermal expansion coefficients of the two constituents of concrete. The thermal expansion coefficient of granite is smaller than that of mortar in the entire range of the investigated values of the RH, compare the Tables 1 and 3. Thus, the largest stress fluctuations are obtained for the largest coefficient of thermal expansion of the mortar, related to $RH = 65\%$.

Stresses in the fine aggregates and the cement paste, see Fig. 15(d) and (e), fluctuate around the stresses in the mortar. These fluctuations are the larger, the greater the difference of the thermal expansion coefficients of the two constituents of mortar. The thermal expansion coefficient of the fine aggregates (limestone) is similar to that of the cement paste at $RH = 100\%$, compare Tables 1 and 3. This explains why the smallest stress fluctuations are obtained for full saturation, compare Fig. 15(b), (d), and (e). The largest difference of the thermal expansion coefficients occurs at $RH = 65\%$, compare Tables 1 and 3. This results in the largest stress fluctuations between the constituents of mortar.

5.3. Sensitivity analysis regarding the speed of the heating process

In order to study the significance of the speed of the temperature change, the duration of the heating process at the top surface of the beam is reduced from 12 to 6 and 3 h, respectively, see Fig. 16(a). The other input quantities remain the same as in Section 4.

The faster the heating process, the larger the curvature of the temperature profiles across the height of the beam (Fig. 16), the smaller the value of the temperature averaged over the cross-sections, and, thus, the smaller the thermal eigenstretch of the beam, see Table 4. Relative to these significant differences, the absolute value of the eigencurvature decreases only slightly with increasing speed of heating, see Table 4. However, the eigenstretch and the eigencurvature do not result in stresses in statically determinate beams.

The faster the heating process, the larger the eigendistortions of the cross-sections of the beam, see Fig. 16(b), and the larger the stresses in the concrete, see Fig. 17(a). Because these stresses are self-equilibrated, compressive stresses are activated at the top and the bottom, and tensile stresses in the central part of the beam, see Fig. 17(a). The stress fluctuations at the two different scales of the microstructure are similar to those discussed in Section 4, see Fig. 17(b)–(e).

5.4. Sensitivity analysis regarding the height of the beam

In order to study the thermoelastic response of concrete beams with different geometric dimensions, the height of the beam is increased from 30 cm to 40 cm and 50 cm, respectively. The other input quantities remain the same as in Section 4.

The larger the height of the beam, the larger the curvature of the temperature profile across the height of the beam after the twelve-hour heating process, see Fig. 18(a). In order to facilitate a comparison, the vertical coordinate is represented in dimensionless form, normalized with respect to the height of the beam, i.e. z/h. With increasing height of the beam, the eigenstretch and the eigencurvature of the beam, according to Eqs. (15) and (17), respectively, are decreasing, see Table 5. However, the eigenstretch and the eigencurvature do not result in stresses in statically determinate beams.

The larger the height of the beam, the larger the eigendistortions of the cross-section of the beam, see Fig. 18(b), and the larger the macroscopic thermal stresses, see Fig. 19(a). The fluctuations of the microstresses are also similar to those discussed in Section 4, see Fig. 19(b)–(e).

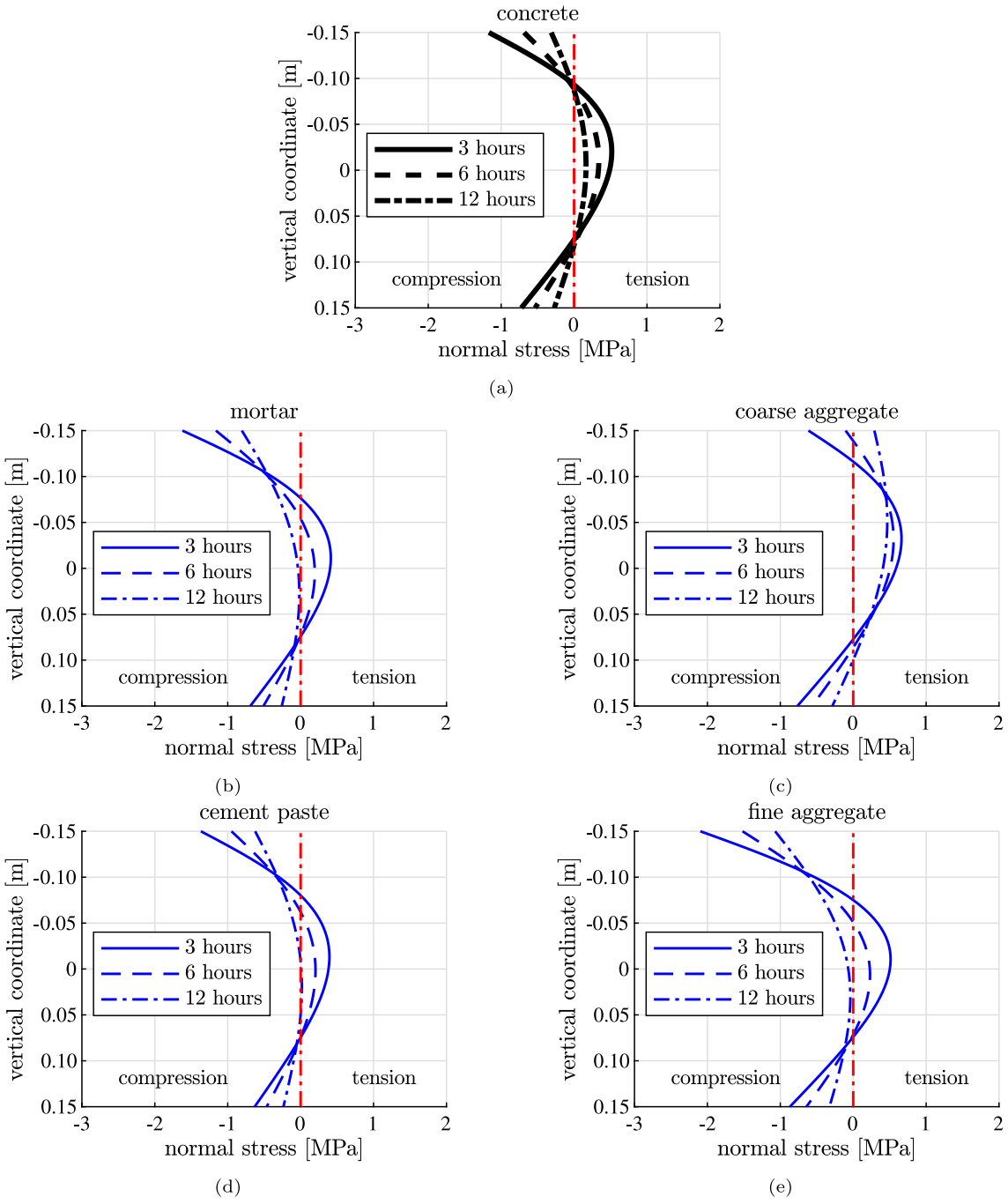

Fig. 17. Results from sensitivity analysis regarding the speed of the heating process: normal stresses in (a) the concrete, (b) the mortar, (c) the coarse aggregates, (d) the cement paste, and (e) the fine aggregates across the height of a statically determinate beam, at the end of three different heating processes, lasting for 12, 6, and 3 h, respectively.

Table 5
Results from sensitivity analysis regarding the height of the beam: eigenstretches and eigencurvatures of the axis of the beam at the end of twelve-hour heating of the top surface.

Height [cm]	ε_0^e [–]	κ_0^e [m^{-1}]
30	5.09×10^{-5}	-3.97×10^{-4}
40	4.25×10^{-5}	-2.91×10^{-4}
50	3.53×10^{-5}	-2.24×10^{-4}

5.5. Implications for long-term durability

Durability of concrete requires the long-term integrity of its microstructure. Interfacial transition zones (ITZ) around the aggregates (Scrivener et al., 2004) are the weakest regions of concrete (Königsberger et al., 2014b). Stresses in the these zones can be computed, using aggregate-to-ITZ stress transfer tensors (Königsberger et al., 2014a), provided that the stress states inside the aggregates are known. These tensors are based on continuity conditions regarding the traction vectors and the displacement vectors across the two-dimensional interface between an aggregate and the surrounding ITZ (Königsberger et al., 2014a).

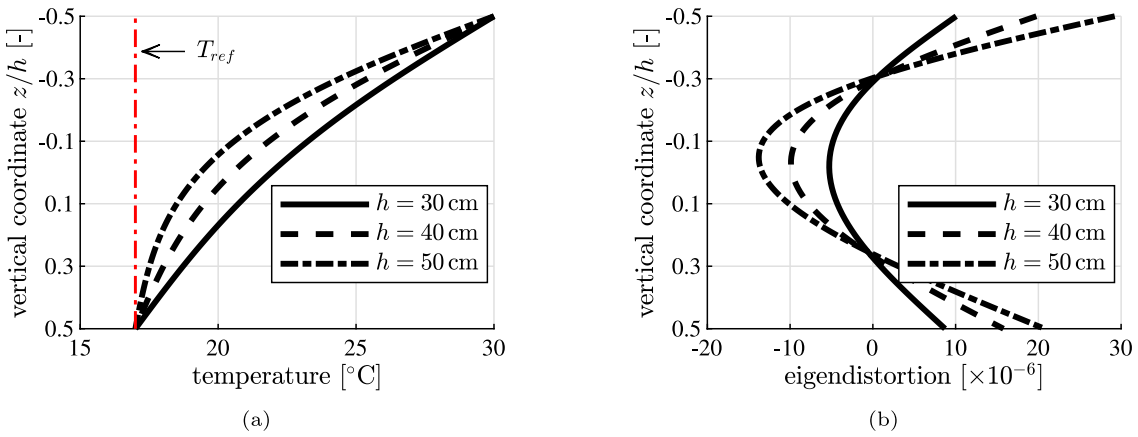

Fig. 18. Results from sensitivity analysis regarding the height of the beam: (a) temperature field and (b) thermal eigendistortions across the height of the beam, at the end of twelve-hour heating of the top surface.

The following discussion refers to statically determinate beams, where the computed thermal normal stresses σ_{xx} at the height of the neutral axis of the beam, $z = 0$, are the total normal stresses even after superposition of the stresses from other load cases resulting in bending, e.g. dead load of the flat roof. The discussion is focused on the two points on the surface of a spherical aggregate, at which the normal vector to the surface is pointing in the direction of $\mathbf{e}_x$. Because of the continuity of the components of the traction vector acting at these surface points, the normal stress σ_{xx} in the aggregate is transferred also to the ITZ. Thus, the normal stresses σ_{xx} in the coarse and the fine aggregates, at $z = 0$, are also acting in the ITZs, see the diagrams (c) and (e) in Figs. 14, 15, and 16. The normal stresses in the ITZs surrounding coarse aggregates are larger than those around fine aggregates, and they are particularly large in case of coarse aggregates made of limestone, see Fig. 14 (c), for an internal relative humidity of 65%, see Fig. 15 (c), and of fast heating of the beam, see Fig. 16 (c). In each one of the three cases, the maximum normal stress is a tensile stress, ranging from 0.60 MPa to 0.80 MPa. This is a significant tensile stress, given that the tensile strength of the ITZ ranges usually from 0.78 MPa to 4.00 MPa (Zimbelmann, 1985; Ping and Beaudoin, 1992; Zhang et al., 2019). It is concluded that daily temperature changes of concrete beams result in daily stress cycles representing a significant fatigue loading of ITZs, particularly in the mid-height region of the beam.

6. Discussion and conclusions

Nonlinear distributions of thermal eigenstrains across the height of a beam are characteristic results of *transient* heat conduction in the thickness direction. The question whether the thermal eigenstrains are free to develop, constrained, or prevented must be answered at different scales of observation: the scale of the entire beam and its specific support conditions, the cross-sectional scale, and the microstructural scales of concrete. In this context, macroscopic thermal eigenstrains of concrete are subdivided into three parts: the eigenstretch of the axis of the beam, its eigencurvature, and the eigendistortion of the cross-sections.

The question whether the eigenstretch and the eigencurvature are free to develop, constrained, or prevented refers to the largest scale of observation. They are only *free* to develop in statically determinate beams. They are at least *constrained* in statically indeterminate beams, depending on the geometric boundary conditions at their supports. In statically indeterminate cases, normal forces and/or bending moments will be activated, leading to linear macroscopic stresses across the height of the beam.

Eigendistortions are *prevented* at the scale of the cross-sections, because the latter remain virtually plane even if the beam is subjected to transient thermal loading. Eigendistortions only vanish in case of stationary heat conduction. Thus, *transient* heat conduction in the thickness direction inevitably leads to macroscopic thermal eigenstresses of concrete, which are nonlinearly distributed across the height of the beam.

Additional constraints refer to microstructural scales of concrete. The mismatch of the thermal expansion coefficients of the constituents of concrete is another source of inevitable thermal eigenstresses. Such stresses are activated even in the seemingly simple case of statically determinate beams subjected to stationary heat conduction. In addition, the mismatch of the elastic stiffness constants of the constituents of concrete results in stress fluctuations. Scale transition methods, taken from continuum micromechanics, were used to quantify microscopic stresses resulting from macroscopic thermal loading.

Microstructural stresses in statically determinate concrete beams are the larger, the faster and the larger the temperature change, and the larger the mismatches of both the thermal expansion coefficients and the elastic stiffness constants of the coarse aggregates, the fine aggregates, and the cement paste matrix. Because the thermal expansion coefficient of the cement paste is a bell-shaped function of the internal relative humidity (Fig. 2), microstructural stresses also depend on the hygral state of the beam.

Daily stress cycles, resulting from diurnal fluctuations of the temperature, represent a recurrent type of loading. Thus, the durability of concrete is reduced, as underlined by thermal tensile stresses of the ITZ, reaching daily maxima ranging from 0.60 MPa to 0.80 MPa at midheight of the beams, noting that the tensile strength of the ITZ ranges usually from 0.78 MPa to 4.00 MPa (Zimbelmann, 1985; Ping and Beaudoin, 1992; Zhang et al., 2019). In order to increase the service life of concrete beams, it is desirable to reduce the amplitudes of the daily cycles of the thermal microstresses. Based on the conclusions of this work, the following recommendations are made:

- It would be beneficial to reduce the difference of the stiffness of the stiff aggregates and the less stiff cement paste matrix. The stiffness of the hardened cement paste can be increased by decreasing the initial water-to-cement mass ratio. This can be achieved, e.g., by using water-reducing agents (= superplasticizers). Aggregates, in turn, are local products, meeting the requirement that transportation distances be reasonably short. Thus, the question whether or not there is a choice between aggregates of different stiffnesses, depends on the local geologic situation. Provided that there is such a choice, it is recommended to use those aggregates which reduce the difference of the stiffness to the hardened cement paste as much as possible.
- It would be beneficial to reduce the difference between the thermal expansion coefficients of the aggregates and the cement

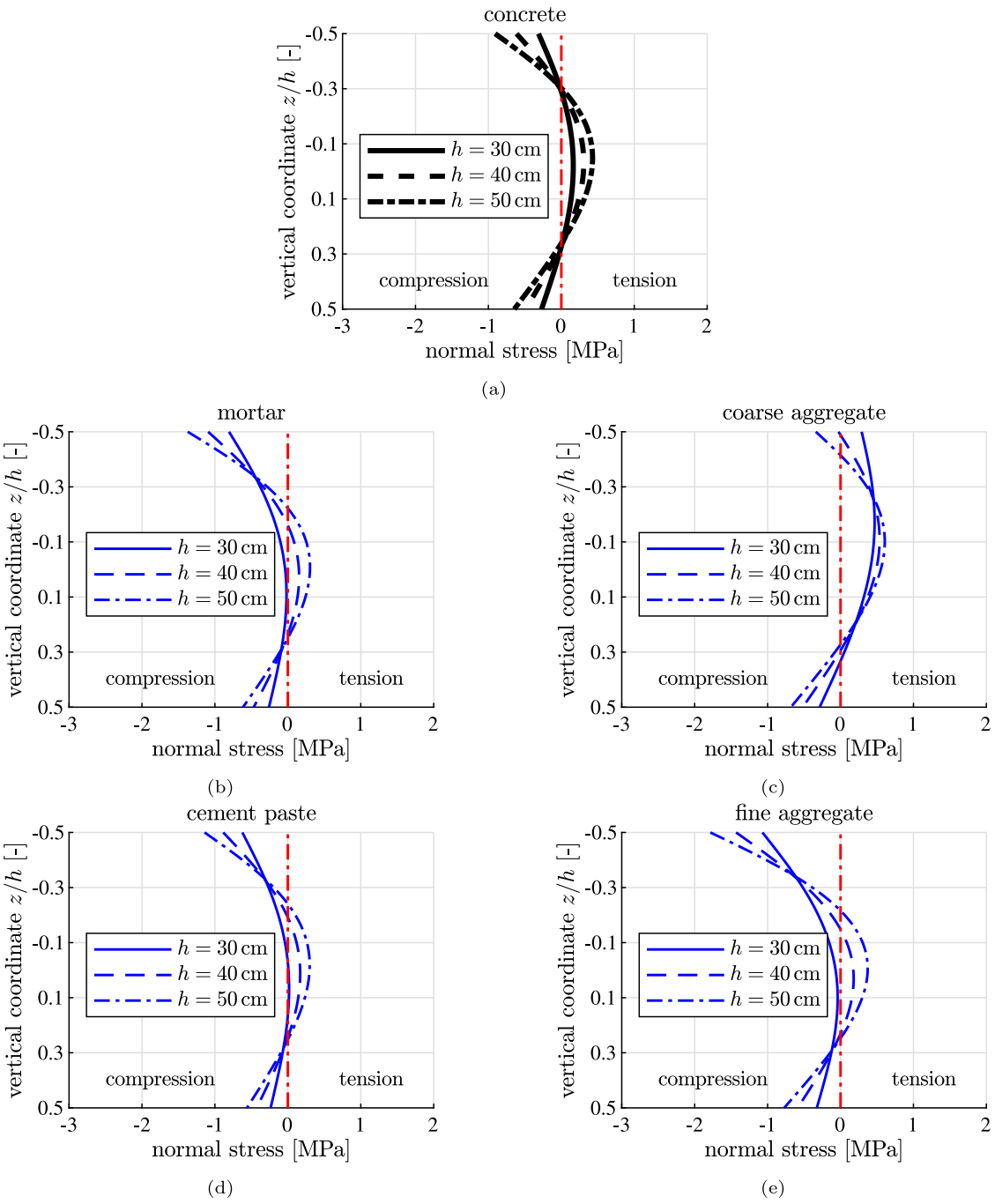

Fig. 19. Results from sensitivity analysis regarding the height of the beam: normal stresses in (a) the concrete, (b) the mortar, (c) the coarse aggregates, (d) the cement paste, and (e) the fine aggregates across the height of a statically determinate beam, at the end of twelve-hour heating of the top surface.

paste matrix. Usual thermal expansion coefficients of aggregates amount to $10\times10^{-6}/°C$ or less. The thermal expansion coefficient of the cement paste is close to $12\times10^{-6}/°C$ for $RH = 0\%$ and $RH = 100\%$. As for relative humidities in the range of 40 to 80%, the thermal expansion coefficient of the cement paste is significantly larger, see Fig. 2. Provided that a choice between different types of aggregates is possible, it is recommended to use those aggregates which reduce the difference of the coefficient of thermal expansion to the cement paste matrix as much as possible. As for the cement paste, it is desirable to avoid RH-values from 40 to 80% e.g. by means of air conditioning systems.

- The best practical remedy for thermal stresses is to reduce the speed and the amplitude of the diurnal thermal loading by means of appropriate insulation. It is concluded that the thermal insulation of flat roofs, as promoted by the United Nations environment program to reduce energy consumption in buildings, is also beneficial to increasing the service life of such roofs by decreasing the amplitude of the daily stress cycles inside the concrete beams that carry the roofs.

Finally, it is noted that the presented results are in good agreement with the ones from previous theoretical, experimental, and numerical studies. The decomposition of the thermal eigenstrains into three parts which are associated with the eigenstretch, the eigencurvature, and the eigendistortions agrees with the decomposition of a nonlinear temperature distribution into a constant, a linear, and a nonlinear part, as proposed in Thomlinson (1940). These theoretical developments have

been used for quantification of thermal eigenstresses of pavement plates based on temperature measurements obtained from in situ monitoring, see e.g. (Choubane and Tia, 1995). Similarly, thermal eigenstresses of pavement plates have also been analyzed by means of Finite Element simulations, see e.g. (Pane et al., 1998; Wang et al., 2019a) and references therein.

CRediT authorship contribution statement

Hui Wang: Investigation, Methodology, Software, Formal analysis, Writing – original draft. **Yong Yuan:** Writing – review & editing, Funding acquisition. **Herbert A. Mang:** Writing – review & editing, Funding acquisition. **Qing Ai:** Writing – review & editing. **Xingchun Huang:** Writing – review & editing. **Bernhard L.A. Pichler:** Conceptualization, Supervision, Writing – review & editing, Project administration.

Declaration of competing interest

The authors declare that they have no known competing financial interests or personal relationships that could have appeared to influence the work reported in this paper.

Acknowledgments

Financial support by the Austrian Science Fund (FWF), provided within project P 281 31-N32 “Bridging the Gap by Means of Multiscale Structural Analyses”, and interesting discussions with Tim Hasenbichler are gratefully acknowledged. The work of the first author is also sponsored by the Shanghai Pujiang Program, China (Grant No. 20PJ1406100).

Appendix. Concentration and influence tensors

The strain concentration tensor of the material phase p reads as (Zaoui, 2002)

$$\mathbb{A}_p = \left[\mathbb{I} + \mathbb{S} : \mathbb{C}_m^{-1} : (\mathbb{C}_p - \mathbb{C}_m)\right]^{-1} : \left\{ \sum_{j=m,i} f_j \left[\mathbb{I} + \mathbb{S} : \mathbb{C}_m^{-1} : (\mathbb{C}_j - \mathbb{C}_m)\right]^{-1} \right\}^{-1}, \quad p \in [m, i], \tag{A.1}$$

The phase-pair eigenstrain influence tensors are taken from (Wang et al., 2019b):

$$\mathbb{D}_{pp} = \left[\mathbb{I} - f_p \mathbb{A}_p\right] : \left[\mathbb{I} + \mathbb{S} : \mathbb{C}_m^{-1} : \left(\mathbb{C}_p - \mathbb{C}_m\right)\right]^{-1} : \left(\mathbb{S} : \mathbb{C}_m^{-1}\right) : \mathbb{C}_p, \tag{A.2}$$

$$\mathbb{D}_{pq} = -\mathbb{A}_p : f_q \left[\mathbb{I} + \mathbb{S} : \mathbb{C}_m^{-1} : \left(\mathbb{C}_q - \mathbb{C}_m\right)\right]^{-1} : \left(\mathbb{S} : \mathbb{C}_m^{-1}\right) : \mathbb{C}_q, \quad p \neq q. \tag{A.3}$$

$\mathbb{S}$ stands for the Eshelby tensor of a spherical inclusion embedded in an infinite matrix of stiffness, $\mathbb{C}_m$. It is given as

$$\mathbb{S} = S_{vol}\, \mathbb{I}_{vol} + S_{dev}\, \mathbb{I}_{dev}, \tag{A.4}$$

with the following expressions for the volumetric and the deviatoric component, S_{vol} and S_{dev}, respectively:

$$S_{vol} = \frac{3\,k_m}{3\,k_m + 4\,\mu_m}, \qquad S_{dev} = \frac{6\,(k_m + 2\,\mu_m)}{5\,(3\,k_m + 4\,\mu_m)}. \tag{A.5}$$

References

ACI Committee 201, 2016. Report 201.2 R-16 – Guide to Durable Concrete. Tech. rep., American Concrete Institute.

Bažant, Z.P., Kaplan, M.F., 1996. Concrete at High Temperatures: Material Properties and Mathematical Models. Longman, Burnt Mill, UK.

Belshe, M., Mamlouk, M.S., Kaloush, K.E., Rodezno, M., 2010. Temperature gradient and curling stresses in concrete pavement with and without open-graded friction course. J. Transp. Eng. 137 (10), 723–729.

Berardi, U., 2017. A cross-country comparison of the building energy consumptions and their trends. Resour. Conserv. Recy. 123, 230–241.

Chen, D., Zou, J., Zhao, L., Xu, S., Xiang, T., Liu, C., 2020. Degradation of dynamic elastic modulus of concrete under periodic temperature-humidity action. Materials 13 (3), 611.

Choubane, B., Tia, M., 1995. Analysis and verification of thermal-gradient effects on concrete pavement. J. Transp. Eng. 121 (1), 75–81.

Dvorak, G.J., 1992. Transformation field analysis of inelastic composite materials. Proc. R. Soc. Lond. Ser. A Math. Phys. Sci. 437 (1900), 311–327.

Emanuel, J.H., Hulsey, J., 1977. Prediction of the thermal coefficient of expansion of concrete. J. Am. Concr. Inst. 74 (4), 149–155.

Fu, Y., Wong, Y., Poon, C., Tang, C., Lin, P., 2004. Experimental study of micro/macro crack development and stress–strain relations of cement-based composite materials at elevated temperatures. Cem. Concr. Res. 34 (5), 789–797.

Grasley, Z.C., 2003. Internal Relative Humidity, Drying Stress Gradients, and Hygrothermal Dilation of Concrete (Ph.D. thesis). University of Illinois at Urbana-Champaign.

Huang, H., An, M., Wang, Y., Yu, Z., Ji, W., 2019. Effect of environmental thermal fatigue on concrete performance based on mesostructural and microstructural analyses. Constr. Build. Mater. 207, 450–462.

Jeong, J.-H., Zollinger, D.G., 2005. Environmental effects on the behavior of jointed plain concrete pavements. J. Transp. Eng. 131 (2), 140–148.

Königsberger, M., Pichler, B., Hellmich, C., 2014a. Micromechanics of ITZ-aggregate interaction in concrete, part I: Stress concentration. J. Am. Ceram. Soc. 97 (2), 535–542.

Königsberger, M., Pichler, B., Hellmich, C., 2014b. Micromechanics of ITZ-aggregate interaction in concrete, part II: Strength upscaling. J. Am. Ceram. Soc. 97 (2), 543–551.

Naik, T., Kraus, R., Kumar, R., 2011. Influence of types of coarse aggregates on the coefficient of thermal expansion of concrete. J. Mater. Civ. Eng. 23 (4), 467–472.

Pane, I., Hansen, W., Mohamed, A., 1998. Three-dimensional finite element study on effects of nonlinear temperature gradients in concrete pavements. Transp. Res. Rec. J. Transp. Res. Board (1629), 58–66.

Pichler, B., Hellmich, C., 2010. Estimation of influence tensors for eigenstressed multiphase elastic media with nonaligned inclusion phases of arbitrary ellipsoidal shape. J. Eng. Mech. 136 (8), 1043–1053.

Ping, X., Beaudoin, J., 1992. Effects of transition zone microstructure on bond strength of aggregate-portland cement paste interfaces. Cem. Concr. Res. 22 (1), 23–26.

Scrivener, K.L., Crumbie, A.K., Laugesen, P., 2004. The interfacial transition zone (ITZ) between cement paste and aggregate in concrete. Interface Sci. 12 (4), 411–421.

The Mathworks, Inc., 2020. MATLAB Version 9.8 (R2020a). Natick, Massachusetts.

Thomlinson, J., 1940. Temperature variations and consequent stresses produced by daily and seasonal temperature cycles in concrete slabs. Concr. Constr. Eng. 36 (6), 298–307.

Wang, H., Binder, E., Mang, H., Yuan, Y., Pichler, B., 2018a. Multiscale structural analysis inspired by exceptional load cases concerning the immersed tunnel of the Hong Kong-Zhuhai-Macao Bridge. Undergr. Space 3 (4), 252–267.

Wang, H., Hellmich, C., Yuan, Y., Mang, H., Pichler, B., 2018b. May reversible water uptake/release by hydrates explain the thermal expansion of cement paste? – Arguments from an inverse multiscale analysis. Cem. Concr. Res. 113, 13–26.

Wang, H., Höller, R., Aminbaghai, M., Hellmich, C., Yuan, Y., Mang, H.A., Pichler, B.L., 2019a. Concrete pavements subjected to hail showers: A semi-analytical thermoelastic multiscale analysis. Eng. Struct. 200, 109677.

Wang, H., Mang, H., Yuan, Y., Pichler, B.L., 2019b. Multiscale thermoelastic analysis of the thermal expansion coefficient and of microscopic thermal stresses of mature concrete. Materials 12 (17), 2689.

Zaoui, A., 2002. Continuum micromechanics: Survey. J. Eng. Mech. 128 (8), 808–816.

Zhang, H., Gan, Y., Xu, Y., Zhang, S., Schlangen, E., Šavija, B., 2019. Experimentally informed fracture modelling of interfacial transition zone at micro-scale. Cem. Concr. Compos. 104, 103383.

Zhao, H., Jiang, K., Yang, R., Tang, Y., Liu, J., 2020. Experimental and theoretical analysis on coupled effect of hydration, temperature and humidity in early-age cement-based materials. Int. J. Heat Mass Transfer 146, 118784.

Zimbelmann, R., 1985. A contribution to the problem of cement-aggregate bond. Cem. Concr. Res. 15 (5), 801–808.